

YU CHENG¹, JONATHAN C. TAN^{1,2}, MENGYAO LIU¹, SHUO KONG³, WANGGI LIM¹, MORTEN ANDERSEN⁴, NICOLA DA RIO¹¹Dept. of Astronomy, University of Florida, Gainesville, Florida 32611, USA²Dept. of Physics, University of Florida, Gainesville, Florida 32611, USA³Dept. of Astronomy, Yale University, New Haven, CT 06511, USA⁴Gemini Observatory, Casilla 603, La Serena, Chile

Draft version June 4, 2024

ABSTRACT

We study the core mass function (CMF) of the massive protocluster G286.21+0.17 with the Atacama Large Millimeter/submillimeter Array via 1.3 mm continuum emission at a resolution of $1.0''$ (2500 au). We have mapped a field of $5.3' \times 5.3'$ centered on the protocluster clump. We measure the CMF in the central region, exploring various core detection algorithms, which give source numbers ranging from 60 to 125, depending on parameter selection. For masses $M \gtrsim 1 M_{\odot}$, the CMF can be fit with a power law of the form $dN/d\log M \propto M^{-\alpha}$ with $\alpha \simeq 1.05 - 1.35$ in the fiducial cases, similar to the index of the Salpeter stellar initial mass function of 1.35. We discuss the implications of these results for star and star cluster formation theories.

Keywords: stars: formation – ISM: clouds

1. INTRODUCTION

The stellar initial mass function (IMF) is of fundamental importance throughout astrophysics. However, in spite of much progress in measuring the IMF (see reviews of, e.g., Bastian et al. 2010; Kroupa et al. 2013), its origin and environmental dependence are still under active debate. Stars are known to form from cold dense cores in molecular clouds. These “prestellar cores” can be defined theoretically as gravitationally-bound, local density maxima that collapse via a single rotationally-supported disk into a single star or small N multiple. In the context of Core Accretion models (e.g., Padoan & Nordlund 2002, 2007; McKee & Tan 2003; Hennebelle & Chabrier 2008; Kunz & Mouschovias 2009), the stellar mass is assumed to be related to the mass of its parental core, modulo a relatively constant core to star formation efficiency, ϵ , perhaps set mostly by outflow feedback (Matzner & McKee 2000; Zhang et al. 2014), with radiative feedback expected to influence only the most massive stars (Tanaka et al. 2017). In this framework, we expect the IMF to be strongly influenced by the prestellar CMF, i.e., the PSCMF. However, there are alternative models, especially Competitive Accretion (Bonnell et al. 2001; Bate 2012), which explain the IMF without a CMF that extends to higher masses. Therefore, the study of the CMF, and ideally the PSCMF, is crucial for understanding the origin of the IMF and its connection to the large-scale physical and chemical conditions of molecular clouds.

Early observations based on submillimeter dust continuum emission (e.g., Motte et al. 1998; Testi & Sargent 1998; Johnstone et al. 2000) found evidence for an approximately log-normal CMF peaking near $\sim 1 M_{\odot}$, with a power law tail at higher masses of the form

$$\frac{dN}{d\log M} \propto M^{-\alpha}. \quad (1)$$

These studies found values of $\alpha \simeq 1.0$ to 1.5, based on samples of several tens of sources. In this form, the Salpeter (1955) $\gtrsim 1 M_{\odot}$ power law fit to stellar masses has an index $\alpha = 1.35$, indicating a potential similarity of the CMF and IMF. Alves et al. (2007) used near-infrared dust extinction to characterize about 160 cores to find similar results, with the peak of the CMF now

better measured close to $1 M_{\odot}$ and the CMF reported to be a simple translation of the IMF requiring $\epsilon \simeq 0.3$. More recent results from the Gould Belt Survey with *Herschel*, *Spitzer* and JCMT have also detected samples of hundreds of cores (e.g., André et al. 2010; Sadavoy et al. 2010; Salji et al. 2015; Marsh et al. 2016) and have added to the evidence for a similarity in shape of the CMF and IMF.

Extending to more distant ($\gtrsim 2$ kpc), high-mass star-forming regions has been more challenging, in particular requiring higher angular resolution interferometric observations. Beuther & Schilke (2004; see also Rodon et al. 2012) reported a CMF of 1.3 mm emission cores in IRAS 19410+2336 ($d \sim 2$ kpc) with $\alpha \simeq 1.5 \pm 0.3$, based on a sample of 24 sources ranging in mass from $\sim 2 - 25 M_{\odot}$. Bontemps et al. (2010) detected a similar number of sources in Cygnus X ($d = 1.7$ kpc), but derived from the follow-up of five quite widely-separated clumps, so that the CMF was not derived from uniform mapping of a contiguous area. Zhang et al. (2015) studied the core population via 1.3 mm emission in the Infrared Dark Cloud (IRDC) G28.34 P1 clump ($d \simeq 5$ kpc) with ALMA, finding 38 cores. They concluded there was a dearth of lower-mass ($\sim 1 - 2 M_{\odot}$) cores compared to the prediction resulting from a scaling down to these masses with a Salpeter mass function. Ohashi et al. (2016) studied the IRDC G14.225-0.506 ($d = 2$ kpc) CMF via 3 mm emission with ALMA at $\sim 3''$ resolution, identifying 48 sources with the clumpfind algorithm (Williams et al. 1994) from two separate fields. They derived $\alpha = 1.6 \pm 0.7$, with the masses ranging from $1.5 - 22 M_{\odot}$.

G286.21+0.17 (hereafter G286) is a massive protocluster associated with the η Car giant molecular cloud at a distance of 2.5 ± 0.3 kpc, in the Carina spiral arm (e.g., Barnes et al. 2010, hereafter B10; Andersen et al. 2017). G286 has been claimed to be $\sim 10^4 M_{\odot}$ (B10), which would make it the most massive and densest of the 300 HCO^+ (1-0) clumps studied by Barnes et al. (2011) and Ma et al. (2013), but an assessment of its dust mass from *Herschel* imaging data suggests a lower mass of $\sim 2000 M_{\odot}$ (Ma et al., in prep.). From modeling of HCO^+ & H^{13}CO^+ spectra, B10 found a global infall rate $\sim 3 \times 10^{-2} M_{\odot} \text{ yr}^{-1}$, one of the largest such infall rates yet measured.

Here we present the ALMA Band 6 (230 GHz) continuum observation of G286 and an analysis of the CMF in this region. This paper is organized as follows: in §2 we describe the observational setup and analysis methods; in §3 we present our results, including an exploration of different analysis techniques for identifying cores and the resulting CMFs; in §4 we discuss and summarize our conclusions.

2. OBSERVATIONS AND ANALYSIS METHODS

2.1. Observational Set-Up

The observations were conducted with ALMA during Cycle 3 (Project ID 2015.1.00357.S, PI: J. C. Tan), during a period from Dec. 2015 to Sept. 2016. To map the entire field of G286 ($\sim 5.3' \times 5.3'$), we divided the region into five strips, denoted as G286_1, G286_2, G286_3, G286_4, and G286_5, each about $1'$ wide and $5.3'$ long and containing 147 pointings of the 12-m array. Figure 1(a) illustrates the spatial extent of the five strips, together with red circles showing the 12-m array mosaic footprints overlaid on strip G286_5 as an example. The position of field center is R.A.=10:38:33, decl.=58:19:22. We employed the compact configuration C36-1 to recover scales between $1.5''$ and $11.0''$. Additionally, a 35-pointing mosaic was performed for each strip using the 7-m array, probing scales up to $18.6''$. Total power observations of the region were also carried out (relevant only for the line observations).

Two scheduling blocks happened to be observed when the array configuration was in a transition phase, i.e., moving from a very extended configuration (C37/C38-1) to our proposed compact configuration. Thus we obtained extra uv coverage for two strips, G286_1 and G286_2, where $\sim 90\%$ of the continuum emission is located. This enables us to detect and characterize structures at a higher resolution ($\sim 1''$, 2500 au) in these regions, which will be the focus of the results presented in this paper.

During the observations, we set the central frequency of the correlator sidebands to be the rest frequency of the $\text{N}_2\text{D}^+(3-2)$ line at 231.32 GHz for SPW0, and the $\text{C}^{18}\text{O}(2-1)$ line at 219.56 GHz for SPW2, with a velocity resolution of 0.046 and 0.048 km s^{-1} , respectively. The second baseband SPW1 was set to 231.00 GHz, i.e., 1.30 mm, to observe continuum with a total bandwidth of 2.0 GHz. The frequency coverage for SPW3 ranges from 215.85 to 217.54 GHz to observe $\text{DCN}(3-2)$, $\text{DCO}^+(3-2)$, $\text{SiO}(v=0)(5-4)$ and $\text{CH}_3\text{OH}(5_{1,4} - 4_{2,2})$. The molecular line data from this observation will be presented and analyzed in a future paper, while here we focus on the results of the broad continuum band, i.e., tracing dust emission.

Both the 7-m and 12-m array data were calibrated with the data reduction pipeline using *Casa* 4.7.0. The continuum visibility data was constructed with all line-free channels. We performed imaging with *tclean* task in *Casa* and during cleaning we combined data for all five strips to generate a final mosaic map. The 7-m array data was imaged using a Briggs weighting scheme with a robust parameter of 0.5, which yields a resolution of $7.32'' \times 4.42''$. For the combined data, we used the same Briggs parameter. In addition, since we have extra uv coverage for part of the data, we also apply a $0.5''$ *wtaper* to suppress

longer baselines, which results in $1.52'' \times 1.41''$ resolution.

The lowest noise level in the image varies from $0.2 \text{ mJy beam}^{-1}$ to $0.46 \text{ mJy beam}^{-1}$, depending on the different strips. The 1σ noise of the central strip is $0.45 \text{ mJy beam}^{-1}$. We also do the cleaning separately for the central two strips with a smaller *wtaper* value to utilize the long baseline data, which results in a resolution of $1.07'' \times 1.02''$. The 1σ noise level in this image is $0.45 \text{ mJy beam}^{-1}$.

2.2. Core Identification

To study the CMF we first need to identify the “cores.” A variety of decomposition algorithms have been used to detect and characterise dense cores in previous studies of continuum maps (e.g., Williams et al. 1994; Kramer et al. 1998; Rosolowsky et al. 2008), and in practice, the results in terms of core number and statistical properties can vary with the different algorithms and input parameters (e.g., Pineda et al. 2009). To understand how the derived CMF depends on these identification methods, we thus adopt two well-documented and widely used algorithms to analyse our data and test the effects of variation of their parameters.

2.2.1. The Dendrogram Method

The dendrogram algorithm is described by Rosolowsky et al. (2008) and implemented in *astrodendro*. The dendrogram is an abstraction of the changing topology of the isosurfaces as a function of contour level. This method can describe hierarchical structures in a 2-D or 3-D datacube. There are two types of structures returned in the results: leaves, which have no sub-structure; and branches, which can split into multiple branches or leaves. Here we only use the leaf structure as a representative of dense cores.

There are three main parameters in this algorithm: F_{\min} , δ , and S_{\min} . First, F_{\min} is the minimum value to be considered in the dataset. In the fiducial case we adopt $F_{\min} = 4\sigma$. Second, δ describes how significant a leaf has to be in order to be considered as an independent entity. We adopt a fiducial value of $\delta = 1\sigma$, which means a core must have a peak flux reaching 5σ above the noise. The minimum area a structure must have to be considered as a core is given by S_{\min} . In general the size of the beam is a good choice, but in a crowded field a detected core can be smaller than one beam size due to blending, especially when a large value of F_{\min} is used. We chose $S_{\min} = 0.5S_{\text{beam}}$. We also explore the effects of varying the choices of F_{\min} , δ , and S_{\min} .

2.2.2. The Clumpfind Method

The clumpfind algorithm (Williams et al. 1994) works by first contouring the data at a multiple of the rms noise of the observation, then searching for peaks of emission that locate the structure, then following them down to lower intensities. It was designed to study molecular clouds using 3-D datacubes and has also been widely used to describe dense cores (e.g., Reid & Wilson 2005; Pineda et al. 2009).

The most sensitive parameters for clumpfind are the lowest contour level (F_{\min}) and level spacing (Δ). F_{\min} is the same as that in the dendrogram method, and we adopt 4σ as a fiducial value. Δ refers to the contour

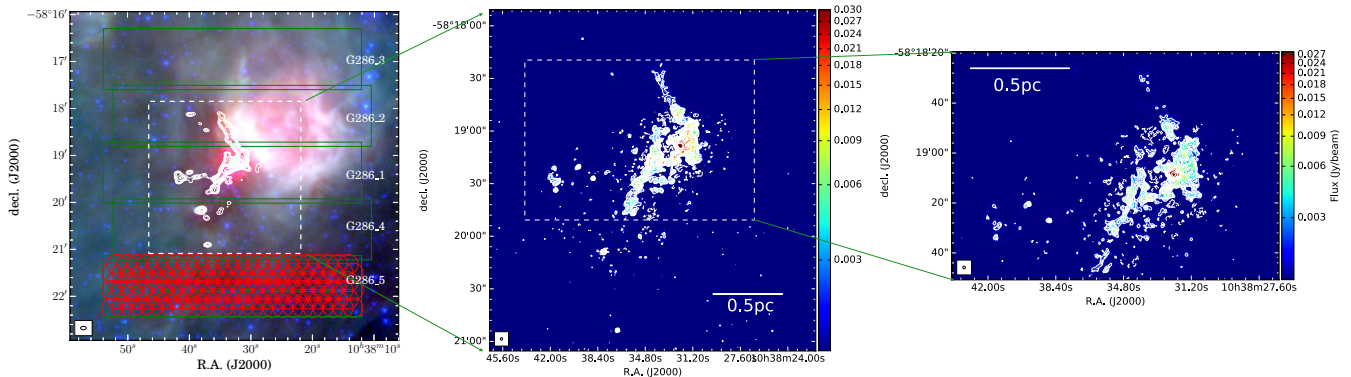


Figure 1. (a) *Left:* Three color image of G286 constructed by combining *Spitzer* IRAC 3.6 μm (blue), 8.0 μm (green), and *Herschel* PACS 70 μm (red). White contours show ALMA 7-m array image starting from 4σ . The G286 field is divided into five strips, as shown by the green rectangles. Each strip is covered with 147 pointings of the 12-m array, illustrated for strip G286_5 as an example with red circles marking the FWHM field of view of each pointing. The white dashed rectangle is the region shown in (b). (b) *Middle:* Image with combined 12-m array and 7-m array data. The resolution is $1.52'' \times 1.41''$. The contour levels are at (4, 8, 10, 12, 15, 20, 25, 30, 40, 50, 75, 100, 150) $\times 0.45 \text{ mJy beam}^{-1}$ (color scale in Jy beam^{-1}). The white dashed rectangle is the region shown in (c). (c) *Right:* Image with combined 12-m array and 7-m array data, but now imaged at $1.07'' \times 1.02''$. Our CMF analysis is carried out for this region.

level spacing and hence is somewhat different from the δ parameter of the dendrogram method. We choose $\Delta = 1\sigma$ in the fiducial case. As with the dendrogram method, cores are required to have a minimum area S_{min} , and we adopt $S_{\text{min}} = 0.5S_{\text{beam}}$ as a fiducial threshold. Again, we investigate the effects of variations in the values of F_{min} , Δ , and S_{min} .

2.3. Core Mass Estimation

We estimate core masses by assuming optically thin thermal emission from dust via the following equation:

$$M = \frac{F_{\nu} d^2}{B_{\nu}(T_{\text{dust}}) \kappa_{\nu}}, \quad (2)$$

where F_{ν} is the total integrated flux, d is the distance to the source, $B_{\nu}(T_{\text{dust}})$ is the Planck function at dust temperature T_{dust} , and κ_{ν} is the dust absorption coefficient.

Since we do not have detailed temperature information for each source, for simplicity we adopt a uniform value of $T_{\text{dust}} = 15 \text{ K}$ for all cores. Such temperatures are expected to be representative of ambient temperatures in dense, prestellar molecular cloud environments (e.g., Pillai et al. 2006; Wang et al. 2008; Chira et al. 2013). However, we recognize that somewhat warmer temperatures may result either from external heating by sources in the embedded protocluster or by internal heating in protostellar cores. If temperatures of 20 K or 30 K are adopted, then this reduces the mass estimates by factors of about 1.5 and 2.5, respectively.

We assume an opacity per unit dust mass $\kappa_{1.2\text{mm},\text{d}} = 1.056 \text{ cm}^2 \text{ g}^{-1}$ (Ossenkopf & Henning 1994), and this gives $\kappa_{1.2\text{mm}} = 7.44 \times 10^{-3} \text{ cm}^2 \text{ g}^{-1}$ using a gas-to-refractory-component-dust ratio of 141 (Draine 2011). For the small offset from 1.2 mm to 1.3 mm of our observation, we scale the opacity via the tabulated frequency dependence of κ_{ν} from Ossenkopf & Henning (1994). Overall, we estimate absolute mass uncertainties of about a factor of two, which we expect to be caused mostly by temperature variations. Relative core mass estimates will be

somewhat more accurate, although still potentially with uncertainties of this magnitude due to temperature and opacity variations between cores.

2.4. Core Recovery Fractions and Completeness Corrections

The core recovery fraction needs to be assessed in order to estimate the completeness level of the “raw” CMF. This completeness is expected to depend on core continuum flux, i.e., mass. It may also depend on core density profile and local environment. In particular, cores in crowded environments will be harder to identify than those in relatively sparse fields.

To assess the core recovery fraction we use a method of inserting artificial cores into the imaging data. The artificial cores are assumed to have the same shape as the synthesized beam, i.e., the limiting case appropriate for small, unresolved cores. The locations of the artificial cores are chosen randomly, but with a probability density that is scaled to match the flux profile we derive from the 7-m array image, which has the effect of placing more cores in crowded regions. In each experiment, we insert 10 cores (i.e., $\sim 10\%$ of the total number to avoid excessive blending) of a given total flux, i.e., of a given mass. We run the core detection algorithms to determine the probability for each artificial core to be found. This is repeated 30 times to obtain a large sample to more accurately assess the recovery fraction. The above steps are repeated for the range of fluxes seen in the raw CMF. Finally, we assume the completeness correction for the raw CMF at a given flux level is equal to the inverse of the recovery fraction, and this is applied to derive the “true” CMF.

3. RESULTS

3.1. 1.3 mm Continuum Image

Figure 1 presents the 1.3 mm continuum map constructed with the 7-m array data in the left panel, 12-m and 7-m array combined data in the middle panel, and the highest resolution combined image in the right panel.

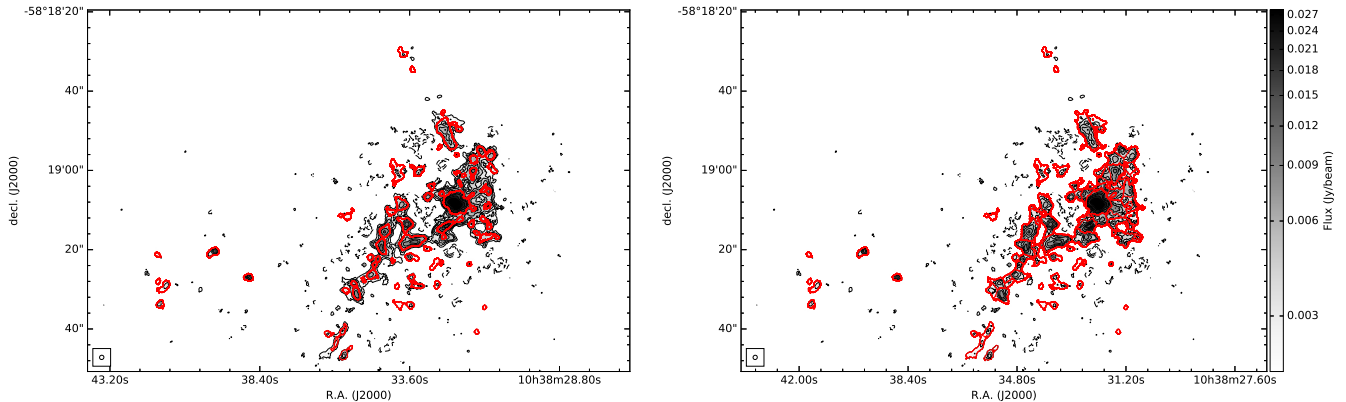


Figure 2. (a) *Left:* Cores found with the dendrogram method using our fiducial criteria: $F_{\min} = 4\sigma$, $\delta = 1\sigma$ and $S_{\min} = 0.5S_{\text{beam}}$. The image is shown in gray scale overlaid on black contours starting from 4σ and increasing in steps of 2σ . The red contours indicate the boundaries of the detected cores. (b) *Right:* Same as (a), but now showing the results of the clumpfind method. The criteria are $F_{\min} = 4\sigma$, $\Delta = 1\sigma$ and $S_{\min} = 0.5S_{\text{beam}}$.

The image with only 7-m data reveals two main filaments: a northern one with a NE–SW orientation and a southern one with a NW–SE orientation. These two filaments converge at a clump with bright mm continuum emission. Several other isolated clumps are also revealed. The southern filament and central hub are further resolved into a cluster of dense cores. The image combining all data has a spatial dynamic range, recovering structures from $\sim 1''$ to $\sim 20''$.

3.2. The Core Population and CMF

Figure 2 shows the high resolution ($\sim 1''$) 1.3 mm continuum image with the core boundaries overlaid for both the dendrogram and clumpfind methods. Inspection of these images allows one to assess how the core identification algorithms operate on the imaging data. One sees cores with a range of sizes, some being many times the size of the beam. Note that the central, brightest and most massive “core” is identified in a similar way with both algorithms. We expect that there is a high probability that such massive, large area “cores” will appear fragmented when imaged at higher angular resolution (see also §4).

Another feature revealed by Figure 2 is clumpfind’s method of partitioning all the flux above the minimum threshold contour level. This is to be contrasted with the method adopted by the dendrogram algorithm, with the effect being to tend to make the cores identified by clumpfind more massive than their dendrogram counterparts.

In Figure 3 we show the “raw” (black histograms) and completeness-corrected “true” (red histograms) CMFs derived from our fiducial dendrogram and clumpfind methods. The CMFs are shown with even binning in $\log M$. Poisson counting errors are shown for each bin. The figure also shows the value of the core recovery fraction, estimated from our artificial core insertion experiments (§2.4).

The fiducial dendrogram method ($F_{\min} = 4\sigma$, $\delta = 1\sigma$, $S_{\min} = 0.5S_{\text{beam}}$) identifies 76 cores. The recovery fraction drops to 1/2 by about $0.6 M_{\odot}$. We characterize the high-end ($> 1.0 M_{\odot}$) part of the CMF by fitting a power law of the form given by equation (1). We find

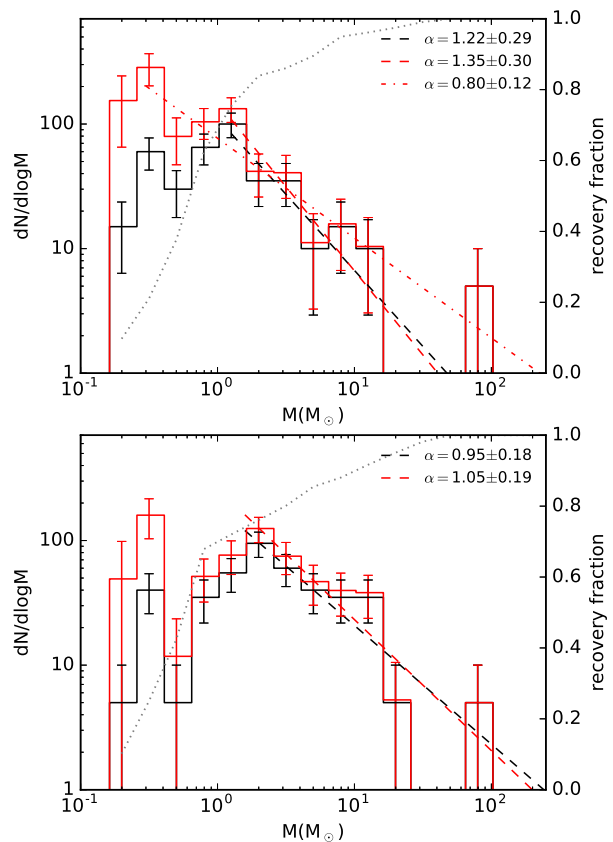


Figure 3. (a) *Top:* Completeness-corrected CMF for the dendrogram method. The CMF before (black) and after completeness correction (red). The black dotted line shows the derived recovery fraction, shown on the right axis (see text). The black dashed line shows the best power law fit result for the high-mass end ($M > 1.5 M_{\odot}$). We also show a tentative fitting result over a wider mass range of $M > 0.2 M_{\odot}$ with the red dashed line. (b) *Bottom:* As (a), but now for the clumpfind method.

$\alpha = 1.22 \pm 0.29$ for the raw CMF. Fitting the same mass range for the completeness-corrected CMF yields $\alpha = 1.35 \pm 0.30$. We note that there is sparse sampling of the high-mass end of the CMF, i.e., there is a single, mas-

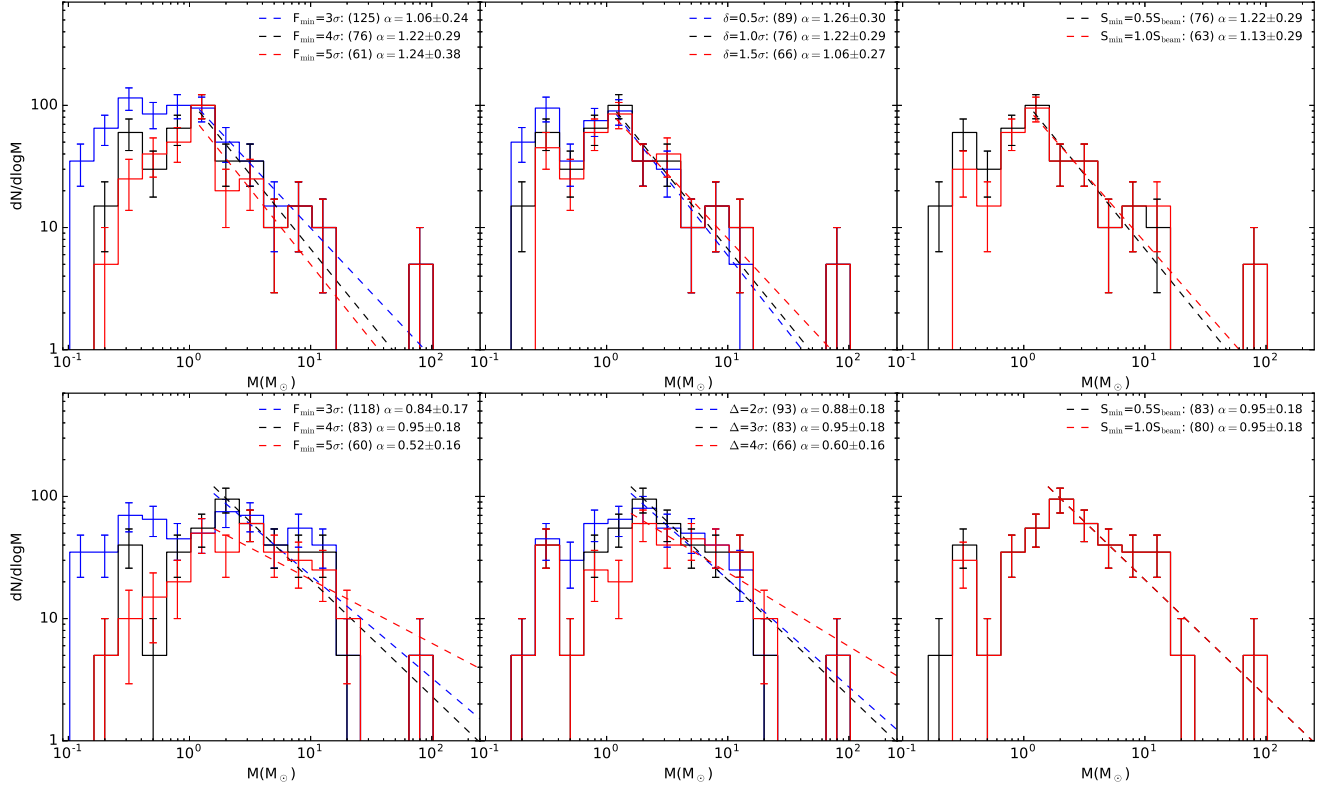


Figure 4. Raw CMFs derived with results from the dendrogram method shown on the top panels, and the clumpfind method on the bottom panels. For each algorithm we show different results by varying F_{\min} , δ (for dendrogram and Δ for clumpfind) and S_{\min} (columns, left to right). In each panel, the results with different parameter selections are illustrated in different colors (see text). The number in the brackets denotes how many cores are detected. Also shown is the power law index, α , from fitting the high-mass end ($M > 1.0 M_{\odot}$ for dendrogram; $M > 1.6 M_{\odot}$ for clumpfind).

sive ($\sim 80 M_{\odot}$) “core.” If we exclude this source and fit the CMF only over the range from 1 to $\sim 15 M_{\odot}$, then we derive $\alpha = 1.26 \pm 0.30$ and $\alpha = 1.38 \pm 0.31$ for the raw and true CMFs, respectively, i.e., there is only a very minor effect. Inspection of the completeness-corrected CMF indicates that the power law behavior may continue down to lower masses. If we fit to the range $M \gtrsim 0.25 M_{\odot}$, we derive a shallower value of $\alpha = 0.80 \pm 0.12$. From these results, we see that there is potential evidence for a break in the CMF near $1 M_{\odot}$, but that a single power law is still a reasonable description of the completeness-corrected CMF across the whole mass range probed, i.e., from $\sim 0.2 M_{\odot}$ to $\sim 80 M_{\odot}$.

The fiducial clumpfind method ($F_{\min} = 4\sigma$, $\Delta = 3\sigma$, $S_{\min} = 0.5S_{\text{beam}}$) finds 83 cores, which then define the raw CMF. The power law description of the raw CMF only appears valid for $M \gtrsim 1.6 M_{\odot}$, and here we derive $\alpha = 0.95 \pm 0.18$. Note, there are a larger number of such massive cores found with the clumpfind method than with the dendrogram method. On applying the completeness correction, the resulting CMF still retains an apparent peak in the CMF at a mass $\sim 2 M_{\odot}$, which contrasts with the dendrogram result that shows only tentative evidence for a break in the power law below $\sim 1 M_{\odot}$. Thus we see that whether or not there is a peak defining a characteristic mass in the CMF depends on the method of core identification used. In particular, while the two methods find similar number of cores, we

can explain the differences in their final CMFs mostly as a result of how mass is then assigned to the identified structures. As discussed above, clumpfind partitions all the flux above a given threshold to the sources, while dendrogram does not, i.e., its cores sit on plateaux that are described by branches in its structural decomposition.

Nevertheless, the values of high-end slopes of the CMFs are relatively robust to the core identification method, with the values of α being consistent with each other given the uncertainties. We note that the stellar IMF at $\gtrsim 1 M_{\odot}$ also follows a power law form with $\alpha \simeq -1.35$ (Salpeter 1955), and this value is very similar to those seen in the CMFs. As previous studies of more local regions have found (see §1), this may indicate that core to star formation efficiency is relatively constant with increasing mass, at least over the range of masses that is effectively probed here, i.e., from ~ 1 to $\sim 20 M_{\odot}$. The outflow and radiative feedback models of Tanaka et al. (2017) for star formation in clumps with $\Sigma_{\text{cl}} \simeq 1 \text{ g cm}^{-2}$, i.e., the value most relevant to G286, predict that these efficiencies should drop from $\epsilon = 0.48$ to 0.37 as the stellar mass increases from $5 M_{\odot}$ to $40 M_{\odot}$, i.e., as core masses increase from about $10 M_{\odot}$ to about $100 M_{\odot}$. Such a relatively small change in ϵ is still compatible with the results we have presented, since they lack significant numbers of cores $> 20 M_{\odot}$ to place very stringent constraints in this regime. Other caveats should also be considered that may affect the derived CMFs, including possible system-

atic temperature variations with increasing continuum flux, i.e., if brighter cores are warmer, we will have over-estimated their masses. However, with the data in hand, it is not currently possible to assess how important this effect may be.

In Figure 4 we show the dependence of the CMFs that result from varying the three main parameters associated with each core identification method. We focus on the total core numbers found, the shape of the raw CMFs, and the high-end slope of the power law fits. In relation to the fiducial dendrogram method, if we lower the minimum threshold to $F_{\min} = 3\sigma$, 125 cores are now found (total core numbers are listed in parentheses in the legend in Fig. 4), with the increase mostly being for sub-solar mass cores. If we set $F_{\min} = 5\sigma$, then 61 cores are recovered. Varying δ to 0.5σ or 1.5σ has a more modest effect, as does increasing the minimum size of a core to 1 beam area. We see from comparing the raw CMFs and their derived values of α (see Fig. 4) that the shape above $1 M_{\odot}$ is relatively robust to these variations. In fact, we note that all the variation we see in α of these raw CMFs due to different dendrogram parameter choices is smaller than the uncertainty arising from Poisson counting statistics in this fiducial estimate.

We have seen that the fiducial clumpfind method yields similar core numbers as the dendrogram analysis. Figure 4 shows that this is also true if we consider variations in its parameters F_{\min} and Δ , in correspondence with the variations of the equivalent dendrogram parameters. However, unlike dendrogram, clumpfind does not see a significant reduction in the numbers of cores found if the minimum core size is doubled. Although most values of the high-end α , here for $M > 1.6 M_{\odot}$, of these raw CMFs are similar to the fiducial value, i.e., 0.95, much lower values, $\sim 0.5 - 0.6$ are derived in some of the cases that find smaller numbers of cores. Such deviations are greater than the uncertainties due to counting statistics and reflect real changes in CMF shapes as fainter, lower-mass sources are removed.

Finally, we examine how the CMFs vary if the analyzed image has a lower angular resolution of $\simeq 1.5''$. Figure 5 compares the raw CMFs derived from the $1''$ and $1.5''$ images. As expected, core masses shift to higher values when identified from the lower resolution image. This leads to a flattening in the shape of the high-end CMFs, i.e., a reduction in the derived values of α , which can be quite significant, i.e., $\Delta\alpha \simeq -(0.3 \text{ to } 0.6)$. This is due to a reduction in number of cores in the lowest mass bin (and a concomitant rise in the numbers in higher-mass bins) of the mass range that is being used to fit the power law. These results indicate that even the high-end part of the CMFs can vary as the resolution is changed, and the trend may continue in the opposite direction if one were to image at higher resolutions. Indeed, this is expected if the more massive, larger cores are seen to fragment at significant levels when imaged at higher resolution. Such cores are known to fragment to some extent, although there are cases of quite limited fragmentation (e.g., Csengeri et al. 2017).

4. DISCUSSION AND CONCLUSIONS

We have studied the CMF in the central region of the massive protocluster G286.21+0.17, with cores identified by their 1.3 mm dust continuum emission in a high spa-

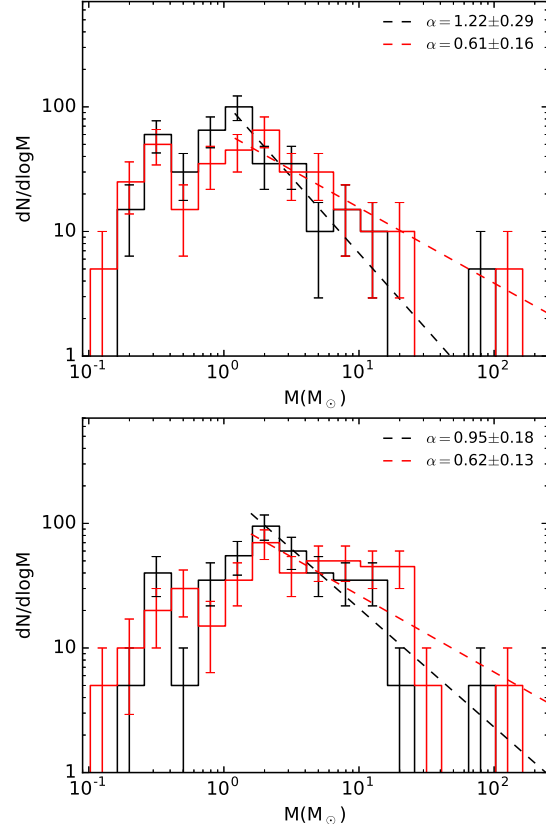


Figure 5. CMFs derived for images with lower spatial resolution ($1.52'' \times 1.41''$) (red histograms) for dendrogram method (upper panel) and clumpfind method (lower panel). The results for our fiducial case, i.e., from the $1.07'' \times 1.02''$ image, are shown in black for comparison.

tial dynamic range image observed with the 7-m and 12-m arrays of ALMA. We explored the effects of using two different core identification algorithms, dendrogram and clumpfind, including a systematic study of varying their three main parameters. We also examined the effects of varying angular resolution of the analyzed continuum image.

Our fiducial methods, including completeness corrections estimated by artificial core insertion and recovery, yield CMFs that show similar high-end power law indices, i.e., $\alpha = 1.35 \pm 0.3$ (dendrogram) to 1.05 ± 0.19 (clumpfind). These values are similar to the Salpeter stellar IMF index of 1.35. This further strengthens the case of a correspondence between CMF and IMF seen in local regions, but now in a more distant, massive protocluster. However, caveats remain, including potential systematic changes in core temperature for brighter cores and the fact that the measured CMF is expected to be composed of a mixture of prestellar and protostellar cores, i.e., tracing different evolutionary stages (see also discussion of Clark et al. 2007).

Considering the variation of CMF properties with analysis method, we find that whether or not a peak is seen in the CMF near $1 M_{\odot}$ depends on if dendrogram or clumpfind is used. Still, even the dendrogram result shows tentative evidence for a break in the power law near this mass. The high-end power law indices are more

robust to the choice of analysis method, but may still vary with the resolution of the image. Fragmentation of “cores” into smaller structures as the resolution is increased has been seen before in numerous studies, but at varying levels (e.g., Beuther & Schilke 2004; Bontemps et al. 2010; Zhang et al. 2015; Csengeri et al. 2017). Cases of limited fragmentation may indicate an important role for magnetic fields in stabilizing the more massive cores (see, e.g., Kunz & Mouschovias 2009; Tan et al. 2013; Fontani et al. 2016).

We re-emphasize that the relation of the CMF identified purely from sub-mm/mm dust continuum emission to the stellar IMF is uncertain. We expect that many of the cores identified by these methods, being the brighter cores, will be protostellar sources. Examples of massive prestellar cores identified by their high levels of deuteration, i.e., via N_2D^+ line emission, can show relatively weak mm continuum emission, perhaps indicating that they are significantly colder than their surrounding clump material (Kong et al. 2017a,b). For constraining theoretical models, it is desirable to have a measure of the PSCMF, and it remains to be seen how effective interferometric studies of mm continuum emission in distant massive protoclusters are at measuring this PSCMF (see, e.g., Fontani et al. 2009).

The observations carried out here also included $N_2D^+(3-2)$ and $^{12}CO(2-1)$, amongst other species. In a future paper, these line data will be analyzed to place better constraints on the PSCMF and its relation to the CMFs presented here. We note that core finding methods that also utilize molecular line emission may also make it easier to break-up spatially confused structures.

Taking the above caveats of CMF definition in mind, we still regard characterization of the mm continuum image via identification of discrete cores by specified, well-defined algorithms as a useful exercise for assessing the fragmentation in the cloud and as a first step for measuring the true CMF and, eventually, the PSCMF. Furthermore, the same core finding algorithms can also be applied to simulated molecular clouds to make a direct, statistical comparison of their structures with real systems, and in this way constrain the physics of star and star cluster formation.

YC acknowledges a Graduate School Fellowship from the University of Florida. JCT acknowledges NSF grants AST1312597 and AST1411527. This paper makes use of the following ALMA data: ADS/JAO.ALMA#2015.1.00357.S. ALMA is a partnership of ESO (representing its member states), NSF (USA) and NINS (Japan), together with NRC (Canada), NSC and ASIAA (Taiwan), and KASI (Republic of Korea), in cooperation with the Republic of Chile. The Joint ALMA Observatory is operated by ESO, AUI/NRAO, and NAOJ. The National Radio Astronomy Observatory is a facility of the National Science Foundation operated under cooperative agreement by Associated Universities, Inc.

REFERENCES

- Alves, J., Lombardi, M., & Lada, C. J. 2007, *A&A*, 462, L17
 Andersen, M., Barnes, P., Tan, J. C., Kainulainen, J. & de Marchi, G. 2017, *AJ*, submitted
 André, P., Men’shchikov, A., Bontemps, S., et al. 2010, *A&A*, 518, L102
 André, P., Di Francesco, J., Ward-Thompson, D., et al. 2014, *Protostars and Planets VI*, 27
 Barnes, P. J., Yonekura, Y., Ryder, S. D., et al. 2010, *MNRAS*, 402, 73
 Barnes, P. J., Yonekura, Y., Fukui, Y. et al. 2011, *ApJS*, 196, 12
 Bastian, N., Covey, K. R., & Meyer, M. R. 2010, *ARA&A*, 48, 339
 Bate M. R. 2012, *MNRAS*, 419, 3115
 Beuther, H., Zhang, Q., Sridharan, T. K., Lee, C.-F., & Zapata, L. A. 2006, *A&A*, 454, 221
 Bonnell I. A. et al. 2001, *MNRAS*, 323, 785.
 Bontemps, S., Motte, F., Csengeri, T., & Schneider, N. 2010, *A&A*, 524, A18
 Chira, R.-A. et al. 2013, *A&A*, 552, 40
 Clark, P. C., Klessen, R. S. & Bonnell, I. A. 2007, *MNRAS*, 379, 57
 Csengeri, T., Bontemps, S., Wyrowski, F. et al. 2017, *A&A*, 600, L10
 Draine B. T. 2011, *Physics of the Interstellar and Intergalactic Medium* (Princeton: Princeton Univ. Press)
 Fontani, F., Commerçon, B., Giannetti, A. et al. 2016, *A&A*, 593, L14
 Fontani, F., Zhang, Q., Caselli, P., & Bourke, T. L. 2009, *A&A*, 499, 233
 Hennebelle, P. & Chabrier, G. 2008, *ApJ*, 684, 395
 Johnstone, D., Wilson, C. D., Moriarty-Schieven, G., et al. 2000, *ApJ*, 545, 327
 Kong, S., Tan, J. C., Caselli, P. et al. 2017a, *ApJ*, 834, 1
 Kong, S., Tan, J. C., Caselli, P. et al. 2017b, *ApJ*, submitted (arXiv:1701.05953)
 Kramer, C., Stutzki, J., Rohrig, R. & Corneliussen, U. 1998, *A&A*, 329, 249
 Kroupa, P., Weidner, C., Pflamm-Altenburg, J., et al. 2013, *Planets, Stars and Stellar Systems. Volume 5: Galactic Structure and Stellar Populations*, 5, 115
 Kunz, M. W. & Mouschovias, T. Ch. 2009, *MNRAS*, 399, L94
 Ma, B., Tan, J. C. & Barnes, P. J. 2013, *ApJ*, 779, 79
 Marsh, K. A., Kirk, J. M., André, P., et al. 2016, *MNRAS*, 459, 342
 Matzner, C. D., & McKee, C. F. 2000, *ApJ*, 545, 364
 McKee, C. F., & Tan, J. C. 2003, *ApJ*, 585, 850
 Motte, F., Andre, P., & Neri, R. 1998, *A&A*, 336, 150
 Nutter, D., & Ward-Thompson, D. 2007, *MNRAS*, 374, 1413
 Ohashi, S., Sanhueza, P., Chen, H.-R. V., et al. 2016, *ApJ*, 833, 209
 Ossenkopf V. & Henning T. 1994, *A&A*, 291, 943
 Padoan, P., & Nordlund, A. 2002, *ApJ*, 576, 870
 Padoan, P., & Nordlund, A. 2007, *ApJ*, 661, 972
 Pillai, T., Wyrowski, F., Carey, S. J., & Menten, K. M. 2006, *A&A*, 450, 569
 Pineda, J. E., Rosolowsky, E. W., & Goodman, A. A. 2009, *ApJ*, 699, L134
 Reid, M. A. & Wilson, C. D. 2005, *ApJ*, 625, 891
 Rodón, J. A., Beuther, H., & Schilke, P. 2012, *A&A*, 545, A51
 Rosolowsky, E. W., Pineda, J. E., Kauffmann, J. & Goodman, A. A. 2008, *ApJ*, 679, 1338
 Sadavoy, S. I., Di Francesco, J., Bontemps, S., et al. 2010, *ApJ*, 710, 1247
 Salji, C. J., Richer, J. S., Buckle, J. V., et al. 2015, *MNRAS*, 449, 1782
 Salpeter, E. E. 1955, *ApJ*, 121, 161
 Tan, J. C., Kong, S., Butler, M. J. et al. 2013, *ApJ*, 779, 96
 Tanaka, K. E. I., Tan, J. C., & Zhang, Y. 2017, *ApJ*, 835, 1
 Testi, L., & Sargent, A. I. 1998, *ApJ*, 508, L91
 Wang Y., Zhang Q., Pillai, T. et al. 2008, *ApJ*, 672, L33
 Williams, J. P., de Geus, E. J., & Blitz, L. 1994, *ApJ*, 428, 693
 Zhang, Q., Wang, K., Lu, X., & Jiménez-Serra, I. 2015, *ApJ*, 804, 141
 Zhang, Y., Tan, J. C. & Hosokawa, T. 2014, *ApJ*, 788, 166